Supplementary Information

1 Band Structure and Topological Invariant Calculation in the TEP-BIC System

To describe the modal coupling and topological properties of the TEP-BIC system, a tight-binding model with four degrees of freedom is established. Considering the periodic coupling between adjacent unit cells, the Bloch Hamiltonians corresponding to the a and b lattice configurations can be written as

$$H_a(k) = \begin{pmatrix} -i\gamma & \kappa & 0 & \kappa e^{-ik} \\ \kappa & +i\gamma & \kappa & 0 \\ 0 & \kappa & +i\gamma & \kappa \\ \kappa e^{ik} & 0 & \kappa & -i\gamma \end{pmatrix}, \tag{1}$$

and

$$H_b(k) = \begin{pmatrix} +i\gamma & \kappa & 0 & \kappa e^{-ik} \\ \kappa & -i\gamma & \kappa & 0 \\ 0 & \kappa & -i\gamma & \kappa \\ \kappa e^{ik} & 0 & \kappa & +i\gamma \end{pmatrix}, \tag{2}$$

where k denotes the Bloch wave vector and κ represents the coupling strength between adjacent sites. The non-Hermiticity of the system originates from the gain–loss modulation term γ, which introduces opposite imaginary onsite potentials into the two types of lattice sites and thereby modifies the imaginary parts of the complex eigenfrequencies.

The above Hamiltonians satisfy the $\mathcal{PT}$-symmetry condition

$$[\mathcal{PT}, H_{a(b)}(k)] = 0. \tag{3}$$

Therefore, variation of the non-Hermitian modulation parameter leads to a continuous evolution of the complex band structure. The corresponding band structure is obtained by solving the eigenvalue equation

$$\left[H_{a(b)}(k) - \omega_n(k)\right] |u_n^R(k)\rangle = 0, \tag{4}$$

where $\omega_n(k)$ denotes the complex eigenvalue of the nth band and $|u_n^R(k)\rangle$ is the corresponding right eigenstate.

By substituting the Hamiltonians in Eqs. (1) and (2), the band structures shown in Fig. S1 are obtained. When $\gamma = 0$, the four-site representation can be regarded as a folded

form of the underlying second-order periodic system. This pseudo-periodicity results in a gapless band structure, with a two-fold degeneracy appearing at the center of the Brillouin zone. When $\gamma \neq 0$, the gain–loss modulation breaks this pseudo-periodicity and lifts the degeneracy. Consequently, a finite spectral gap develops between the target bands, providing the spectral basis for the subsequent formation and evolution of the non-Hermitian interface states.

To characterize the topological property associated with this band evolution, the two target bands involved in the band exchange are selected and analyzed using a biorthogonal Wilson loop. Since the Hamiltonian is non-Hermitian,

$$H_{a(b)}(k) \neq H_{a(b)}^{\dagger}(k), \tag{5}$$

the left and right eigenstates are generally different and must be treated separately. The right eigenstates are defined through

$$H_{a(b)}(k)|u_n^R(k)\rangle = \omega_n(k)|u_n^R(k)\rangle, \tag{6}$$

whereas the corresponding left eigenstates satisfy

$$\langle u_n^L(k)|H_{a(b)}(k) = \omega_n(k)\langle u_n^L(k)|. \tag{7}$$

The left and right eigenstates are normalized according to the biorthogonal condition

$$\langle u_m^L(k)|u_n^R(k)\rangle = \delta_{mn}. \tag{8}$$

In the numerical calculation, the complete set of right eigenstates of the four-dimensional Bloch Hamiltonian is first collected into the eigenstate matrix

$$V_R(k) = \left(|u_1^R(k)\rangle, |u_2^R(k)\rangle, |u_3^R(k)\rangle, |u_4^R(k)\rangle\right). \tag{9}$$

For a diagonalizable Hamiltonian, the corresponding complete left-eigenstate matrix can then be constructed from

$$V_L(k) = \left[V_R^{-1}(k)\right]^{\dagger}. \tag{10}$$

This construction guarantees the biorthogonal normalization of the complete left and right eigenbases. After obtaining the full eigenstate matrices, the left and right eigenvectors corresponding to the two target bands are selected to construct the Wilson loop. In this way, the matrix inversion is performed on the complete four-dimensional eigenbasis, while the topological invariant is evaluated only within the two-band subspace of interest.

For two adjacent Bloch wave vectors k_i and k_{i+1}, the biorthogonal overlap matrix within the selected band subspace is defined as

$$F_{mn}(k_i, k_{i+1}) = \langle u_m^L(k_i) | u_n^R(k_{i+1}) \rangle, \tag{11}$$

where m and n run over the two target bands. The entire Brillouin zone is discretized into M sampling points according to

$$k_i = i\Delta k, \tag{12}$$

with

$$\Delta k = \frac{2\pi}{M}. \tag{13}$$

Because the Wilson loop is defined over a closed path in the Brillouin zone, the final sampling point is connected back to the initial one, i.e., $k_{M+1} \equiv k_1$. The Wilson-loop matrix is therefore obtained by accumulating the overlap matrices along the closed Brillouin-zone path,

$$W = \prod_{i=1}^{M} F(k_i, k_{i+1}). \tag{14}$$

The eigenvalues of the Wilson-loop matrix are then calculated from

$$W|\phi_j\rangle = \lambda_j |\phi_j\rangle, \tag{15}$$

where λ_j denotes the jth Wilson-loop eigenvalue. The corresponding Wannier center is obtained from the phase of λ_j as

$$\nu_j = -\frac{i}{2\pi} \ln(\lambda_j). \tag{16}$$

This quantity is used to characterize the topology of the selected two-band subspace. The calculated evolution of the Wannier center under variation of the non-Hermitian modulation parameter γ is shown in Fig. S2(a).

For both the a and b lattice configurations, the calculated Wannier centers coincide at $\nu = 0.5$ for nonzero γ, corresponding to a nontrivial biorthogonal geometric phase of π, as shown in Fig. S2(a). This result indicates that the selected band subspaces of both configurations retain their nontrivial topology under non-Hermitian modulation. The point at $\gamma = 0$ corresponds to the Hermitian band-touching limit and is distinguished from the gapped non-Hermitian regime at finite γ.

For comparison, a non-Hermitian lattice with a different arrangement of the gain–loss onsite potentials is further considered. Its Bloch Hamiltonian is written as

$$H'(k) = \begin{pmatrix} -i\gamma & \kappa & 0 & \kappa e^{-ik} \\ \kappa & -i\gamma & \kappa & 0 \\ 0 & \kappa & +i\gamma & \kappa \\ \kappa e^{ik} & 0 & \kappa & +i\gamma \end{pmatrix}. \tag{17}$$

The same biorthogonal Wilson-loop procedure is applied to this comparison system. As shown in Fig. S2(b), the corresponding Wannier center is $\nu = 0$, indicating a topologically trivial band subspace. This result provides a direct comparison with the $\nu = 0.5$ target-band subspace of the TEP-BIC lattice and confirms that the latter carries a nontrivial biorthogonal geometric phase.

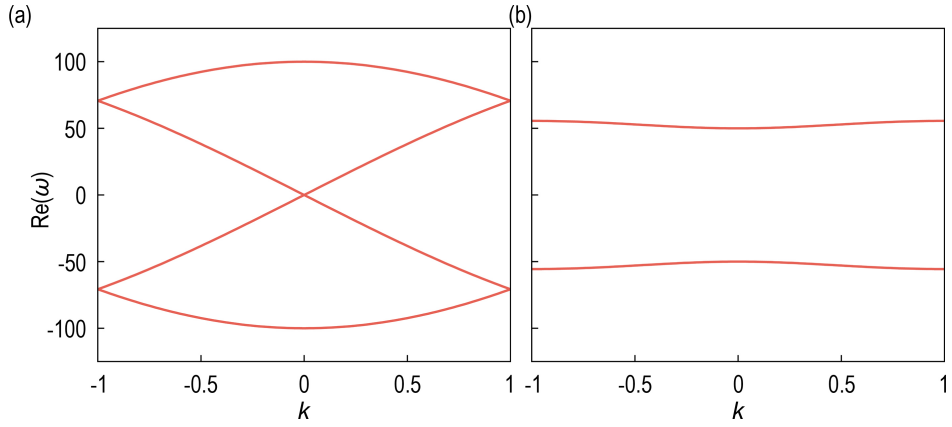


FIG. S1. Band structures of the four-site lattice under different non-Hermitian modulation strengths γ.

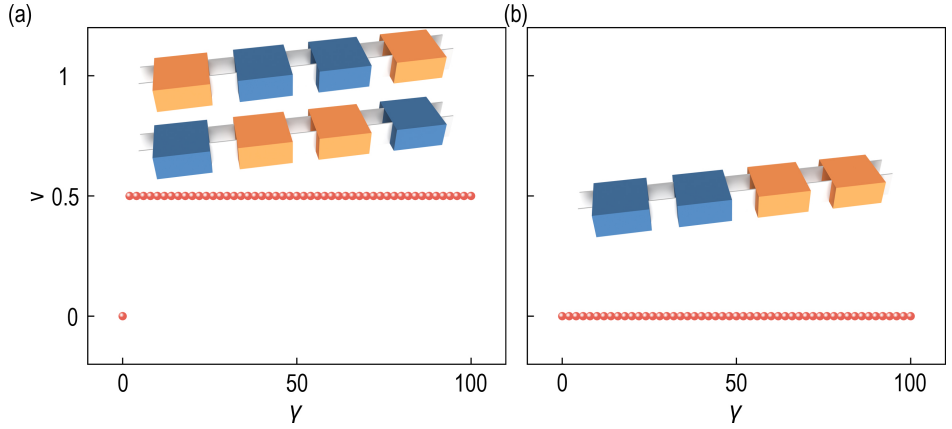


FIG. S2. Topological invariant calculation based on the biorthogonal Wilson loop. (a) Evolution of the Wannier centers calculated for the a and b lattice configurations as a function of the non-Hermitian modulation parameter γ. The results of the two configurations overlap at $\nu = 0.5$ for nonzero γ. (b) Wannier center of the comparison non-Hermitian lattice described by Eq. (17).

2 Equivalence Between Cavity-Ordered and Mode-Separated Hamiltonian Representations

Consider a finite acoustic chain composed of N coupled rectangular cavities. Each cavity supports two mutually orthogonal acoustic modes, denoted by the σ and π modes. The nth cavity therefore contains two modal degrees of freedom,

$$|n,\sigma\rangle, \qquad |n,\pi\rangle. \tag{18}$$

In the physical acoustic structure, these two modal degrees of freedom belong to the same cavity. It is therefore natural to first arrange the basis according to the cavity index. Under this cavity-ordered representation, the state vector is written as

$$\Psi_c = \left(|1,\sigma\rangle, |1,\pi\rangle, |2,\sigma\rangle, |2,\pi\rangle, \ldots, |N,\sigma\rangle, |N,\pi\rangle\right)^T. \tag{19}$$

The acoustic chain consists of two types of non-Hermitian cavities. The A cavity represents the gain unit, whereas the B cavity represents the loss unit. Their corresponding non-Hermitian onsite corrections are defined as

$$\gamma_n = \begin{cases} +\gamma, & A \text{ cavity}, \\ -\gamma, & B \text{ cavity}. \end{cases} \tag{20}$$

Consistent with the lattice convention adopted in Section 1, the a configuration follows the (B, A, A, B) sequence. Therefore, within the mth unit cell,

$$\gamma_n^{(a)} = \begin{cases} -\gamma, & n = 4m+1,\ 4m+4, \\ +\gamma, & n = 4m+2,\ 4m+3. \end{cases} \tag{21}$$

The b configuration follows the complementary (A, B, B, A) sequence,

$$\gamma_n^{(b)} = \begin{cases} +\gamma, & n = 4m+1,\ 4m+4, \\ -\gamma, & n = 4m+2,\ 4m+3. \end{cases} \tag{22}$$

The two orthogonal modes experience the same local gain–loss modulation within a given cavity, while their unperturbed modal frequencies can in general be different. The local Hamiltonian of the nth cavity can therefore be written as

$$h_n = \begin{pmatrix} f_\sigma + i\gamma_n & 0 \\ 0 & f_\pi + i\gamma_n \end{pmatrix}, \tag{23}$$

where f_σ and f_π denote the uncoupled eigenfrequencies of the two modal sectors. If the Hamiltonian is expressed relative to the corresponding modal reference frequencies, these

constant diagonal terms can equivalently be omitted without affecting the following basis transformation.

For the symmetry-preserving coupling geometry considered here, coupling between adjacent cavities occurs only between modes of the same modal character. The cross-mode coupling matrix elements between the σ and π sectors therefore vanish. The inter-cavity coupling block is written as

$$\mathcal{K} = \begin{pmatrix} \kappa_\sigma & 0 \\ 0 & \kappa_\pi \end{pmatrix}, \tag{24}$$

where κ_σ and κ_π are the nearest-neighbor coupling strengths associated with the σ and π modes, respectively.

Under the cavity-ordered basis, the Hamiltonian of the finite acoustic chain takes the block-tridiagonal form

$$H_c = \begin{pmatrix} h_1 & \mathcal{K} & 0 & \cdots & 0 \\ \mathcal{K} & h_2 & \mathcal{K} & \ddots & \vdots \\ 0 & \mathcal{K} & h_3 & \ddots & 0 \\ \vdots & \ddots & \ddots & \ddots & \mathcal{K} \\ 0 & \cdots & 0 & \mathcal{K} & h_N \end{pmatrix}. \tag{25}$$

This representation directly follows the physical ordering of the cavities and simultaneously contains the non-Hermitian modulation associated with the A/B cavity sequence and the two modal coupling channels. Although no σ–π conversion is present in H_c, the two modal degrees of freedom are interleaved in the basis ordering,

$$(\sigma_1, \pi_1, \sigma_2, \pi_2, \ldots, \sigma_N, \pi_N), \tag{26}$$

and the separation between the two independent modal sectors is therefore not explicit in this representation.

To reveal this structure, a permutation matrix P is introduced to reorder the degrees of freedom. The transformed state vector is defined as

$$\Psi_m = P\Psi_c, \tag{27}$$

with the new basis ordering

$$\Psi_m = (|1,\sigma\rangle, |2,\sigma\rangle, \ldots, |N,\sigma\rangle, |1,\pi\rangle, |2,\pi\rangle, \ldots, |N,\pi\rangle)^T. \tag{28}$$

The transformation does not mix any physical degrees of freedom and only changes their ordering. Since P is a permutation matrix,

$$P^{-1} = P^{\dagger}, \tag{29}$$

and the Hamiltonian in the mode-separated basis is therefore

$$H_m = PH_cP^{-1} = PH_cP^{\dagger}. \tag{30}$$

After the permutation, all σ-mode degrees of freedom are grouped into one subspace and all π-mode degrees of freedom into the other. Because the original Hamiltonian contains no cross-mode coupling terms, the transformed Hamiltonian becomes block diagonal,

$$H_m = \begin{pmatrix} H_\sigma & 0 \\ 0 & H_\pi \end{pmatrix}, \tag{31}$$

or equivalently,

$$H_m = H_\sigma \oplus H_\pi. \tag{32}$$

The two modal Hamiltonians are explicitly given by

$$H_\sigma = \begin{pmatrix} f_\sigma + i\gamma_1 & \kappa_\sigma & 0 & \cdots \\ \kappa_\sigma & f_\sigma + i\gamma_2 & \kappa_\sigma & \cdots \\ 0 & \kappa_\sigma & f_\sigma + i\gamma_3 & \cdots \\ \vdots & \vdots & \vdots & \ddots \end{pmatrix}, \tag{33}$$

and

$$H_\pi = \begin{pmatrix} f_\pi + i\gamma_1 & \kappa_\pi & 0 & \cdots \\ \kappa_\pi & f_\pi + i\gamma_2 & \kappa_\pi & \cdots \\ 0 & \kappa_\pi & f_\pi + i\gamma_3 & \cdots \\ \vdots & \vdots & \vdots & \ddots \end{pmatrix}. \tag{34}$$

Thus, the original cavity-ordered Hamiltonian is transformed exactly into the direct sum of two independent non-Hermitian chains. The first chain contains all σ-mode degrees of freedom and is governed by f_σ and κ_σ, whereas the second contains all π-mode degrees of freedom and is governed by f_π and κ_π. Importantly, this separation is mathematically exact within the effective Hamiltonian considered here, where the cross-mode coupling terms vanish under the symmetry-preserving coupling configuration.

To demonstrate explicitly that the two representations are algebraically equivalent, we compare their characteristic equations. Since

$$H_m = PH_cP^{\dagger}, \tag{35}$$

the characteristic polynomial satisfies

$$\begin{aligned}\det(\omega I_{2N} - H_m) &= \det(\omega I_{2N} - P H_c P^\dagger) \\ &= \det\left[P(\omega I_{2N} - H_c)P^\dagger\right] \\ &= \det(P)\det(\omega I_{2N} - H_c)\det(P^\dagger).\end{aligned} \tag{36}$$

For a permutation matrix,

$$\det(P)\det(P^\dagger) = |\det(P)|^2 = 1, \tag{37}$$

and therefore

$$\det(\omega I_{2N} - H_m) = \det(\omega I_{2N} - H_c). \tag{38}$$

Consequently,

$$\mathrm{Spec}(H_m) = \mathrm{Spec}(H_c). \tag{39}$$

The permutation therefore leaves all eigenvalues unchanged. Since $H_m = H_\sigma \oplus H_\pi$, the same spectrum can simultaneously be written as the union of the spectra of the two modal subspaces,

$$\mathrm{Spec}(H_c) = \mathrm{Spec}(H_\sigma) \cup \mathrm{Spec}(H_\pi). \tag{40}$$

The equivalence also applies directly to the eigenstates. If a right eigenstate of the cavity-ordered Hamiltonian satisfies

$$H_c|\psi_c^R\rangle = \omega|\psi_c^R\rangle. \tag{41}$$

then

$$\begin{aligned}H_m P|\psi_c^R\rangle &= P H_c P^\dagger P|\psi_c^R\rangle \\ &= P H_c|\psi_c^R\rangle \\ &= \omega P|\psi_c^R\rangle.\end{aligned} \tag{42}$$

Therefore, the corresponding right eigenstate in the mode-separated basis is

$$|\psi_m^R\rangle = P|\psi_c^R\rangle. \tag{43}$$

Similarly, for a left eigenstate satisfying

$$\langle\psi_c^L|H_c = \omega\langle\psi_c^L|. \tag{44}$$

the transformed left eigenstate is

$$\langle \psi_m^L | = \langle \psi_c^L | P^\dagger. \tag{45}$$

Hence, neither the eigenvalues nor the physical eigenstates are altered by the transformation; only the ordering of their components is changed. The biorthogonal structure of the non-Hermitian eigenstates is likewise preserved under the permutation.

Therefore, the cavity-ordered representation H_c and the mode-separated representation $H_\sigma \oplus H_\pi$ are strictly algebraically equivalent. The former directly reflects the physical arrangement of the acoustic cavities, whereas the latter makes the two independent modal sectors explicit. This equivalence provides the theoretical basis for treating the σ- and π-mode spectra independently while retaining their exact correspondence to the same physical acoustic lattice. It is this mode-separated representation that allows the localized non-Hermitian interface states of one modal sector and the bulk continuum of the orthogonal modal sector to be analyzed within a common physical system.

3 Non-Hermitian Band Gap Evolution and Generation of Topological Interface States

After establishing the nontrivial topological property of the target-band subspace, we further investigate how the non-Hermitian modulation parameter γ modifies the complex spectrum and the associated interface states. For a finite chain, the eigenvalue problem can be written as

$$H_{a(b)}\Psi_n = \omega_n \Psi_n, \tag{46}$$

where

$$\omega_n = \omega_n^{\mathrm{R}} + i\omega_n^{\mathrm{I}} \tag{47}$$

denotes the complex eigenfrequency of the nth eigenstate. Because the spectrum is complex, the real and imaginary parts of the eigenfrequencies provide two complementary descriptions of the spectral structure. The real part ω_n^{R} describes the resonance-frequency distribution, whereas the imaginary part ω_n^{I} reflects the non-Hermitian gain–loss evolution of the corresponding mode. Therefore, spectral gaps can be formed independently in the real and imaginary components of the complex eigenfrequency.

When $\gamma = 0$, the gain–loss modulation vanishes and the system reduces to the Hermitian limit. As shown in Fig. S3(a), the folded bands touch and no finite non-Hermitian spectral gap is present around the target frequency. Correspondingly, the interface-state branches discussed below are not spectrally isolated from the bulk bands in either the real or imaginary part of the spectrum.

As the non-Hermitian modulation is introduced and gradually increased, the complex bands evolve continuously. The first prominent change appears in the real part of the spectrum, where the originally touching bulk branches separate and form a finite gap in the real part of the spectrum. As shown in Fig. S3(b), a pair of interface-localized states appears inside this real-part gap. Their real eigenfrequencies lie between the neighboring bulk branches, while their spatial distributions are localized around the domain wall between the two lattice configurations. We denote these states as $\mathrm{ES}_{\mathrm{Re}}$ to indicate that their spectral isolation is associated primarily with the gap formed in the real part of the complex spectrum.

With a further increase in γ, the imaginary parts of the bulk eigenfrequencies also reorganize. When the modulation reaches $\gamma = \kappa$, a gap in the imaginary part of the complex spectrum begins to open, as shown in Fig. S3(c). This condition also marks the localization threshold of the corresponding interface-state branches. For $\gamma > \kappa$, these states become exponentially localized around the domain wall and are spectrally separated from the bulk states in the imaginary-frequency direction. We denote these states by $\mathrm{ES}_{\mathrm{Im}}$. In contrast to

$\mathrm{ES}_{\mathrm{Re}}$, whose spectral isolation is associated with the real-part gap, $\mathrm{ES}_{\mathrm{Im}}$ is directly connected to the non-Hermitian reorganization of the imaginary spectrum.

The value $\gamma = \kappa$ should be distinguished from the exceptional-point condition discussed below. In the present model, $\gamma = \kappa$ marks the onset of the imaginary-part spectral gap and, as will be shown analytically in the following section, also corresponds to the localization threshold of the relevant interface-state solution. The exceptional point occurs only at a larger modulation strength, when the two interface-state eigenvalues and their corresponding eigenvectors coalesce.

As γ increases, the opening of the real-part spectral gap is accompanied by the emergence of $\mathrm{ES}_{\mathrm{Re}}$, followed by the formation of the imaginary-part spectral gap and the localization of $\mathrm{ES}_{\mathrm{Im}}$ beyond the threshold $\gamma = \kappa$.

The subsequent evolution of $\mathrm{ES}_{\mathrm{Im}}$ is particularly important for the formation of the exceptional point. As γ continues to increase beyond the localization threshold, the two interface-state eigenvalues approach each other in the complex-frequency plane. At

$$\gamma = \sqrt{2}\kappa, \tag{48}$$

the two eigenvalues coalesce, producing the exceptional point shown in Fig. S3(d). When the non-Hermitian modulation is increased further, the eigenvalues separate again, but now along the imaginary-frequency direction, as shown in Fig. S3(e). The analytical origin of this evolution, including the localization condition and the exceptional-point condition, is derived explicitly in the following section.

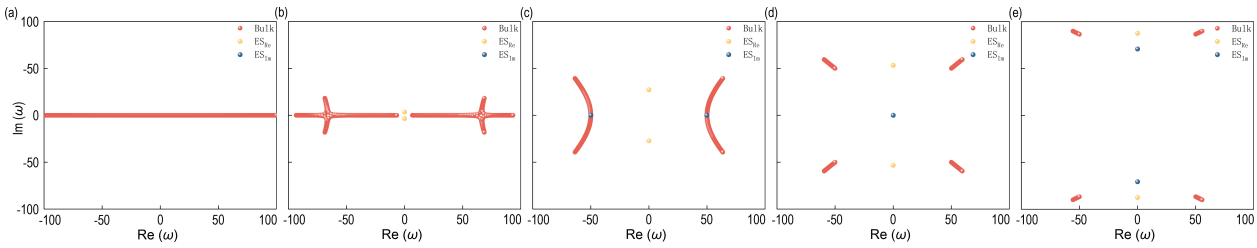


FIG. S3. Evolution of the non-Hermitian spectral gaps and interface states in the TEP-BIC system. (a) Complex spectrum at $\gamma = 0$, where no finite non-Hermitian spectral gap is present around the target frequency. (b) Opening of the real-part spectral gap and emergence of the corresponding interface states $\mathrm{ES}_{\mathrm{Re}}$. (c) Onset of the imaginary-part spectral gap at $\gamma = \kappa$, marking the localization threshold of $\mathrm{ES}_{\mathrm{Im}}$. (d) Coalescence of the two interface-state eigenvalues at $\gamma = \sqrt{2}\kappa$, corresponding to the exceptional point. (e) Splitting of the interface-state eigenvalues along the imaginary direction when $\gamma > \sqrt{2}\kappa$.

4 Analytical Derivation of the Topological Interface States

To further derive the eigenvalues and spatial localization of the topological interface states, the finite-chain eigenvalue equation is considered in the site basis. For the nth cavity, the eigenvalue equation can be written as

$$\kappa\Psi_{n-1} + i\gamma_n\Psi_n + \kappa\Psi_{n+1} = \omega\Psi_n, \tag{49}$$

where Ψ_n denotes the acoustic-mode amplitude at the nth cavity, ω represents the eigenfrequency relative to the reference cavity frequency, κ is the nearest-neighbor coupling strength, and γ_n denotes the local non-Hermitian modulation.

Consistent with the Bloch Hamiltonians introduced in Section 1, the non-Hermitian modulation of the a lattice configuration is distributed as

$$\gamma_n^{(a)} = \begin{cases} -\gamma, & n = 4m+1,\ 4m+4, \\ +\gamma, & n = 4m+2,\ 4m+3, \end{cases} \tag{50}$$

whereas for the b lattice configuration,

$$\gamma_n^{(b)} = \begin{cases} +\gamma, & n = 4m+1,\ 4m+4, \\ -\gamma, & n = 4m+2,\ 4m+3. \end{cases} \tag{51}$$

To describe the spatial evolution of the eigenmodes, we define the two-component state vector

$$\mathbf{v}_n = \begin{pmatrix} \Psi_n \\ \Psi_{n-1} \end{pmatrix}. \tag{52}$$

The discrete eigenvalue equation can then be rewritten in the transfer-matrix form

$$\mathbf{v}_{n+1} = T_n\mathbf{v}_n, \tag{53}$$

where

$$T_n = \begin{pmatrix} \dfrac{\omega - i\gamma_n}{\kappa} & -1 \\ 1 & 0 \end{pmatrix}. \tag{54}$$

For the two possible onsite modulations, the corresponding single-site transfer matrices are

$$T_+ = \begin{pmatrix} \dfrac{\omega - i\gamma}{\kappa} & -1 \\ 1 & 0 \end{pmatrix}, \tag{55}$$

and

$$T_- = \begin{pmatrix} \dfrac{\omega + i\gamma}{\kappa} & -1 \\ 1 & 0 \end{pmatrix}, \tag{56}$$

where T_+ and T_- correspond to $\gamma_n = +\gamma$ and $\gamma_n = -\gamma$, respectively.

Taking the positive x direction from left to right, the transfer matrix over one complete period of the a lattice configuration is

$$M_a = T_- T_+ T_+ T_-, \tag{57}$$

while that of the b configuration is

$$M_b = T_+ T_- T_- T_+. \tag{58}$$

Although the two configurations possess different spatial sequences of the gain–loss modulation, their bulk transfer matrices have the same characteristic equation. In particular,

$$\det(T_+) = \det(T_-) = 1, \tag{59}$$

and therefore

$$\det(M_a) = \det(M_b) = 1. \tag{60}$$

Direct evaluation further gives

$$\mathrm{Tr}(M_a) = \mathrm{Tr}(M_b) = \frac{\omega^4 + 2\omega^2\gamma^2 - 4\omega^2\kappa^2 + \gamma^4 + 2\kappa^4}{\kappa^4}. \tag{61}$$

If λ denotes an eigenvalue of the period transfer matrix, the corresponding transfer eigenmode satisfies

$$M_{a(b)} \mathbf{v}_n = \lambda \mathbf{v}_n, \tag{62}$$

or equivalently,

$$\mathbf{v}_{n+4} = \lambda \mathbf{v}_n. \tag{63}$$

Since the determinant of the period transfer matrix is unity, its two eigenvalues form a reciprocal pair, λ and λ^{-1}. Consequently, the bulk transfer relation for both lattice configurations is

$$\lambda + \lambda^{-1} = \frac{\omega^4 + 2\omega^2\gamma^2 - 4\omega^2\kappa^2 + \gamma^4 + 2\kappa^4}{\kappa^4}. \tag{64}$$

This relation describes the spatial evolution of the eigenmodes in the periodic bulk regions. To obtain the interface-state solution, the matching condition between the two lattice configurations must additionally be satisfied.

We consider an a–b interface, with the a configuration occupying the left side and the b configuration occupying the right side. The positive x direction is defined from the left lattice toward the right lattice. The amplitudes in the unit cell immediately to the left of the interface are denoted by

$$(a, b, c, d)^T, \tag{65}$$

whereas those in the adjacent unit cell on the right are denoted by

$$(p, q, r, s)^T. \tag{66}$$

For an interface-localized solution, the state must decay toward both semi-infinite bulk regions. We therefore denote by β the forward transfer eigenvalue in the right-hand bulk and choose the branch satisfying

$$|\beta| < 1. \tag{67}$$

Because the two bulk transfer eigenvalues are reciprocal, the corresponding forward transfer eigenvalue in the left-hand bulk is β^{-1}. Thus, when all transfer relations are defined along the same positive x direction, the right-hand amplitudes satisfy $\mathbf{v}_{j+1} = \beta \mathbf{v}_j$, whereas the left-hand amplitudes satisfy $\mathbf{v}_{j+1} = \beta^{-1}\mathbf{v}_j$. Consequently, the unit cell immediately preceding the left interface cell carries amplitudes scaled by β, while the unit cell immediately following the right interface cell is also scaled by β. This common representation allows the matching equations on the two sides of the interface to be written using the same parameter β without introducing different spatial coordinate directions.

The eigenvalue equations for the two unit cells adjacent to the interface are therefore

$$\kappa\beta d - i\gamma a + \kappa b = \omega a, \tag{68}$$

$$\kappa a + i\gamma b + \kappa c = \omega b, \tag{69}$$

$$\kappa b + i\gamma c + \kappa d = \omega c, \tag{70}$$

$$\kappa c - i\gamma d + \kappa p = \omega d, \tag{71}$$

$$\kappa d + i\gamma p + \kappa q = \omega p, \tag{72}$$

$$\kappa p - i\gamma q + \kappa r = \omega q, \tag{73}$$

$$\kappa q - i\gamma r + \kappa s = \omega r, \tag{74}$$

and

$$\kappa r + i\gamma s + \kappa\beta p = \omega s. \tag{75}$$

These equations can be written compactly as

$$M(\omega,\beta)\begin{pmatrix} a \\ b \\ c \\ d \\ p \\ q \\ r \\ s \end{pmatrix} = 0, \tag{76}$$

where

$$M(\omega,\beta) = \begin{pmatrix} -i\gamma-\omega & \kappa & 0 & \kappa\beta & 0 & 0 & 0 & 0 \\ \kappa & i\gamma-\omega & \kappa & 0 & 0 & 0 & 0 & 0 \\ 0 & \kappa & i\gamma-\omega & \kappa & 0 & 0 & 0 & 0 \\ 0 & 0 & \kappa & -i\gamma-\omega & \kappa & 0 & 0 & 0 \\ 0 & 0 & 0 & \kappa & i\gamma-\omega & \kappa & 0 & 0 \\ 0 & 0 & 0 & 0 & \kappa & -i\gamma-\omega & \kappa & 0 \\ 0 & 0 & 0 & 0 & 0 & \kappa & -i\gamma-\omega & \kappa \\ 0 & 0 & 0 & 0 & \kappa\beta & 0 & \kappa & i\gamma-\omega \end{pmatrix}. \tag{77}$$

For a nontrivial interface solution, the determinant of the coefficient matrix must vanish,

$$\det M(\omega,\beta) = 0. \tag{78}$$

At the same time, β must satisfy the bulk transfer relation. Since β is one of the reciprocal bulk transfer eigenvalues, the corresponding polynomial equation is

$$\beta^2 - \frac{\omega^4 + 2\omega^2\gamma^2 - 4\omega^2\kappa^2 + \gamma^4 + 2\kappa^4}{\kappa^4}\beta + 1 = 0. \tag{79}$$

The simultaneous solutions of the interface matching condition and the bulk transfer relation contain several algebraic branches. Among them, the pair corresponding to the central interface states considered in this work is

$$\omega_{\mathrm{int},\pm} = \pm\sqrt{2\kappa^2 - \gamma^2}. \tag{80}$$

This pair is the branch that evolves into the localized interface states discussed below. Substituting this result into the bulk transfer relation gives

$$\begin{aligned} \beta + \beta^{-1} &= \frac{(2\kappa^2 - \gamma^2)^2 + 2(2\kappa^2 - \gamma^2)\gamma^2}{-4(2\kappa^2 - \gamma^2)\kappa^2 + \gamma^4 + 2\kappa^4} \\ &= 4\left(\frac{\gamma}{\kappa}\right)^2 - 2. \end{aligned} \tag{81}$$

Multiplying by β leads to

$$\beta^2 - \left[4\left(\frac{\gamma}{\kappa}\right)^2 - 2\right]\beta + 1 = 0. \tag{82}$$

The two transfer roots are therefore

$$\beta_\pm = \left[\frac{\gamma}{\kappa} \pm \sqrt{\left(\frac{\gamma}{\kappa}\right)^2 - 1}\right]^2. \tag{83}$$

For $0 \le \gamma < \kappa$, the two roots form a complex-conjugate reciprocal pair with unit magnitude, $|\beta_\pm| = 1$, and therefore do not produce exponential localization. At $\gamma = \kappa$, the two transfer roots merge at $\beta = 1$. When $\gamma > \kappa$, the two roots become real and reciprocal, and the root satisfying $|\beta| < 1$ is

$$\beta_{\mathrm{int}} = \left[\frac{\gamma}{\kappa} - \sqrt{\left(\frac{\gamma}{\kappa}\right)^2 - 1}\right]^2. \tag{84}$$

The interface-state amplitude therefore decays exponentially into the two bulk regions when $\gamma > \kappa$. Accordingly, $\gamma = \kappa$ marks the localization threshold of this interface-state branch.

The localization condition should be distinguished from the exceptional-point condition. The latter is determined by the coalescence of the two interface-state eigenvalues and their eigenvectors. From

$$\omega_{\mathrm{int},\pm} = \pm\sqrt{2\kappa^2 - \gamma^2}, \tag{85}$$

the two eigenvalues become degenerate when

$$\gamma_{\mathrm{EP}} = \sqrt{2}\kappa, \tag{86}$$

at which

$$\omega_{\mathrm{int},+} = \omega_{\mathrm{int},-} = 0. \tag{87}$$

At the same point, the localized transfer factor is

$$\beta_{\mathrm{EP}} = (\sqrt{2}-1)^2 = 3 - 2\sqrt{2}, \tag{88}$$

which satisfies $|\beta_{\mathrm{EP}}| < 1$, confirming that the degenerate state remains exponentially localized at the interface.

To determine the geometric multiplicity of this degeneracy, we substitute

$$\omega = 0, \qquad \gamma = \sqrt{2}\kappa, \qquad \beta = 3 - 2\sqrt{2} \tag{89}$$

into the interface matching equation $M(\omega, \beta)\Psi = 0$. Solving the resulting linear system gives, up to an arbitrary normalization factor C, a single independent right eigenstate,

$$|\Psi_{\mathrm{EP}}\rangle = C \begin{pmatrix} i \\ -(1+\sqrt{2}) \\ i(1+\sqrt{2}) \\ 3+2\sqrt{2} \\ i(3+2\sqrt{2}) \\ 1+\sqrt{2} \\ -i(1+\sqrt{2}) \\ 1 \end{pmatrix}. \tag{90}$$

Equivalently, the coefficient matrix at the degeneracy satisfies

$$\operatorname{rank} M(0, 3-2\sqrt{2}) = 7, \tag{91}$$

and therefore

$$\dim \ker M(0, 3-2\sqrt{2}) = 1. \tag{92}$$

Thus, although the two interface-state eigenvalue branches become degenerate at $\omega = 0$, only one linearly independent eigenvector remains. The degeneracy therefore has algebraic multiplicity two but geometric multiplicity one, demonstrating that $\gamma = \sqrt{2}\kappa$ corresponds to a second-order exceptional point.

For the parameter range

$$\kappa < \gamma < \sqrt{2}\kappa, \tag{93}$$

the interface states are exponentially localized and their eigenvalues remain real,

$$\omega_{\mathrm{int},\pm} = \pm\sqrt{2\kappa^2 - \gamma^2}. \tag{94}$$

At

$$\gamma = \sqrt{2}\kappa, \tag{95}$$

the two localized interface states coalesce at the exceptional point. When the non-Hermitian modulation is further increased,

$$\gamma > \sqrt{2}\kappa, \tag{96}$$

the interface-state eigenvalues split along the imaginary direction and become

$$\omega_{\mathrm{int},\pm} = \pm i\sqrt{\gamma^2 - 2\kappa^2}. \tag{97}$$

Therefore, the spatial localization and exceptional-point conditions are governed by two distinct properties of the interface solution. The onset of localization is determined by the magnitude of the bulk transfer eigenvalue and occurs at $\gamma = \kappa$, whereas the exceptional point is determined by the simultaneous coalescence of the interface eigenvalues and eigenvectors at $\gamma = \sqrt{2}\kappa$.

5 Evolution of the Imaginary-Gap Interface States toward the Exceptional Point

The non-Hermitian spectral evolution discussed above gives rise to two different types of interface states. As the gain–loss modulation is introduced, a band gap first opens in the real part of the bulk spectrum, within which a pair of interface states appears. With a further increase in the non-Hermitian modulation strength, the imaginary part of the bulk spectrum is reorganized and an additional band gap opens in the imaginary-frequency direction. A second pair of interface states then appears within this imaginary-part band gap. In the following discussion, the two types of interface states are referred to as $\mathrm{ES}_{\mathrm{Re}}$ and $\mathrm{ES}_{\mathrm{Im}}$, respectively, according to the part of the complex spectrum in which they are spectrally isolated.

The two pairs of interface states exhibit different spectral evolutions as the non-Hermitian modulation parameter γ is increased. The $\mathrm{ES}_{\mathrm{Re}}$ states remain associated with the band gap formed in the real part of the spectrum and do not evolve into the exceptional degeneracy considered in this work. In contrast, the $\mathrm{ES}_{\mathrm{Im}}$ states emerge together with the opening of the imaginary-part band gap and continue to evolve strongly with the non-Hermitian modulation. It is this latter pair of interface states that eventually undergoes both eigenvalue and eigenvector coalescence and forms the exceptional point.

The analytical derivation in the previous section shows that the eigenvalues of the relevant interface-state pair are

$$\omega_{\mathrm{int},\pm} = \pm\sqrt{2\kappa^2 - \gamma^2}. \tag{98}$$

At $\gamma = \kappa$, a gap begins to open in the imaginary part of the bulk spectrum. At the same parameter value, the transfer-factor analysis identifies the localization threshold of the corresponding interface-state branch. For $\gamma > \kappa$, one of the reciprocal transfer roots satisfies $|\beta| < 1$, and the associated interface states become exponentially localized around the a–b domain wall. Therefore, the localization of $\mathrm{ES}_{\mathrm{Im}}$ is directly associated with the opening of the imaginary-part spectral gap.

Within the parameter range

$$\kappa < \gamma < \sqrt{2}\kappa, \tag{99}$$

the two $\mathrm{ES}_{\mathrm{Im}}$ states remain localized at the interface, while their eigenvalues remain real and continuously approach each other as γ increases. This evolution corresponds to the progressive convergence of the two interface-state branches shown in Fig. S3(c)–(d). Although the states are already spatially localized in this regime, their eigenvalues are still distinct, and the exceptional degeneracy has not yet been reached.

When the non-Hermitian modulation reaches

$$\gamma = \sqrt{2}\kappa, \tag{100}$$

the two interface-state eigenvalues merge at

$$\omega_{\mathrm{int},+} = \omega_{\mathrm{int},-} = 0. \tag{101}$$

The interface matching analysis presented in the previous section further shows that the coefficient matrix at this point has rank seven. Since the matching problem contains eight interface amplitudes, only one linearly independent nonzero solution remains. Therefore, the two interface-state branches not only become degenerate in eigenvalue but also share the same eigenvector. The degeneracy is thus a second-order exceptional point.

This result establishes the spectral origin of the exceptional point in the present system. Rather than being introduced as an independent degeneracy, the EP is reached through the continuous evolution of the pair of $\mathrm{ES}_{\mathrm{Im}}$ states that emerges after the imaginary-part band gap is opened. The formation of the imaginary-part band gap first provides the spectral region in which the relevant interface states become localized, and the subsequent increase in γ continuously drives their eigenvalues toward coalescence.

When the non-Hermitian modulation is increased beyond the exceptional point,

$$\gamma > \sqrt{2}\kappa, \tag{102}$$

the square root in the interface-state eigenvalue becomes imaginary, and the two branches evolve as

$$\omega_{\mathrm{int},\pm} = \pm i\sqrt{\gamma^2 - 2\kappa^2}. \tag{103}$$

The coalesced eigenvalue therefore splits again along the imaginary-frequency direction, as shown in Fig. S3(e). The corresponding states remain localized around the interface because the localization condition $\gamma > \kappa$ continues to be satisfied. Their post-EP evolution is thus still governed by the imaginary part of the non-Hermitian spectrum.

The complete evolution of the exceptional interface states can therefore be understood as a continuous process. The opening of the imaginary-part band gap is accompanied by the formation and localization of the $\mathrm{ES}_{\mathrm{Im}}$ states. These two interface-state branches then approach each other with increasing γ and coalesce at $\gamma = \sqrt{2}\kappa$, forming the second-order exceptional point. Beyond this point, the two branches separate along the imaginary-frequency direction while remaining localized at the domain wall. This evolution demonstrates that the exceptional point in the TEP-BIC system originates from the coalescence of the interface states associated with the imaginary-part band gap.

6 Geometric Parameters of the Physical Acoustic Lattice

To map the idealized tight-binding model onto a physical acoustic platform, the finite lattice is constructed from rectangular cavities coupled through connecting necks. The system consists of 24 cavities, forming an a–b domain wall with three four-cavity supercells arranged on each side of the interface.

The geometric configuration and corresponding parameter definitions are illustrated in Fig. S4. The cavity dimensions along the three spatial directions are denoted by l_x, l_y, and l_z, respectively. The connecting-neck length and height are denoted by l_n and h_n, respectively. The connecting necks are positioned at 0.25 and 0.75 of the cavity height, measured from the bottom of the cavity.

The reference cavity dimension is defined as $l_0 = 40$ mm, and the geometric detuning between the two orthogonal modal directions is given by $\Delta l = l_y - l_x$. For the TEP-BIC configuration, $l_x = 40$ mm and $\Delta l = -0.32$ mm, corresponding to $l_y = 39.68$ mm. The outer-shell thickness of the fabricated cavities is 3 mm.

The geometric parameters of the physical acoustic lattice are summarized in Table S1. These parameters determine the modal frequencies and inter-cavity coupling strengths, whose quantitative relationships are further discussed in Section 7.

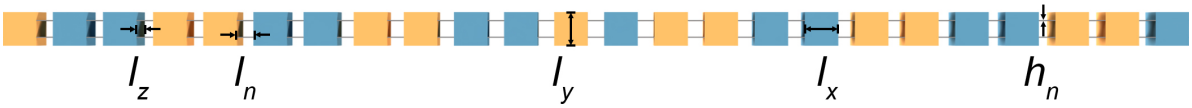


FIG. S4. Geometric parameters of the physical acoustic lattice. The schematic illustrates the finite acoustic cavity array and the geometric definitions of the cavity dimensions l_x, l_y, and l_z, as well as the connecting-neck length l_n and height h_n. The connecting necks are located at 0.25 and 0.75 of the cavity height. The corresponding parameter values are summarized in Table S1.

Table S1: Geometric parameters of the physical acoustic lattice.

Symbol	Description	Value
l_x	Cavity dimension along the x direction	40 mm
l_y	Cavity dimension along the y direction	39.68 mm
l_z	Cavity dimension along the z direction	20 mm
l_n	Connecting-neck length	20 mm
h_n	Connecting-neck height	1 mm
t_s	Outer-shell thickness	3 mm

7 Band Structure Regulation

For the TEP-BIC system, the structural parameters of the acoustic cavities can be directly related to the parameters of the effective Hamiltonian through numerical fitting. The modal frequencies and inter-cavity coupling strengths are first extracted in the Hermitian limit, $\gamma = 0$, where the influence of the geometric parameters can be identified independently from the non-Hermitian modulation. The resulting fitted parameters are subsequently used in the general non-Hermitian Hamiltonian.

For the σ-mode sector of the a lattice configuration, the effective Hamiltonian, including the eigenfrequency of the uncoupled cavity mode, can be written as

$$H_a^{(\sigma)}(k) = \begin{pmatrix} -i\gamma & \kappa_\sigma & 0 & \kappa_\sigma e^{-ik} \\ \kappa_\sigma & +i\gamma & \kappa_\sigma & 0 \\ 0 & \kappa_\sigma & +i\gamma & \kappa_\sigma \\ \kappa_\sigma e^{ik} & 0 & \kappa_\sigma & -i\gamma \end{pmatrix} + f_\sigma I, \tag{104}$$

where f_σ denotes the eigenfrequency of the isolated σ mode and κ_σ represents the corresponding nearest-neighbor coupling strength. With the other structural parameters fixed, the σ-mode frequency and coupling strength are found to depend approximately linearly on the cavity dimension l_x:

$$f_\sigma = 4282.2 - 107.0(l_x - l_0), \tag{105}$$

$$\kappa_\sigma = 65.0 - 43.9(l_x - l_0). \tag{106}$$

Similarly, the effective Hamiltonian of the π-mode sector can be written as

$$H_a^{(\pi)}(k) = \begin{pmatrix} -i\gamma & \kappa_\pi & 0 & \kappa_\pi e^{-ik} \\ \kappa_\pi & +i\gamma & \kappa_\pi & 0 \\ 0 & \kappa_\pi & +i\gamma & \kappa_\pi \\ \kappa_\pi e^{ik} & 0 & \kappa_\pi & -i\gamma \end{pmatrix} + f_\pi I, \tag{107}$$

where f_π and κ_π denote the eigenfrequency and nearest-neighbor coupling strength of the π-mode sector, respectively. The corresponding π-mode frequency and coupling strength are related to l_y by

$$f_\pi = 4282.2 - 108.3(l_y - l_0), \tag{108}$$

and

$$\kappa_\pi = 33.3 - 3.1(l_y - l_0). \tag{109}$$

Here, $l_0 = 40$ mm denotes the reference cavity dimension. In the above fitting relations, l_x, l_y, and l_0 are expressed in millimeters, whereas f_σ, f_π, κ_σ, and κ_π are expressed in hertz. These relations establish a direct quantitative connection between the geometric dimensions of the acoustic cavity and the onsite modal frequencies and inter-cavity coupling strengths in the effective Hamiltonian. Consequently, the relative spectral positions of the two orthogonal modal sectors can be controlled through geometric tuning of l_x and l_y.

7.1 Spectral Evolution under Geometric Detuning

To characterize the relative geometric tuning between the two orthogonal modal directions, we define

$$\Delta l = l_y - l_x. \tag{110}$$

In the geometric tuning shown in Fig. S5, l_x is fixed at the reference value $l_0 = 40$ mm, while $l_y = l_0 + \Delta l$ is varied. In this tuning process, varying l_y modifies f_π and κ_π, while l_x, f_σ, and κ_σ remain fixed. The parameter Δl therefore characterizes the relative geometric detuning between the σ-mode and π-mode sectors and provides a direct means of shifting their spectra with respect to each other. During this tuning process, the two modal sectors retain their distinct σ- and π-mode characters, allowing the relative positions of their bulk states and interface states to be continuously adjusted.

Figure S5 shows the complete spectral evolution of the finite lattice as Δl is varied. The bulk spectra and the corresponding interface states of the σ and π sectors move relative to one another, producing several characteristic spectral configurations. These configurations are identified as TEP-BIC, TBIC_1, Topological Fano (TF), and TBIC_2 in Fig. S5(a). Although all four configurations originate from the relative spectral displacement of the two orthogonal modal sectors, they correspond to different relationships between the interface states and the surrounding bulk continua.

In the TEP-BIC regime, the two σ-mode interface-state branches reach their exceptional-point condition and coalesce, while the corresponding eigenfrequency is simultaneously embedded within the bulk continuum of the orthogonal π-mode sector. The state therefore combines the exceptional degeneracy of the σ-mode interface states with the continuum embedding provided by the π-mode bulk states. Owing to the orthogonality between the two modal sectors, the continuum embedding does not by itself introduce direct hybridization between the coalesced σ-mode state and the surrounding π-mode bulk states.

The TBIC_1 and TBIC_2 regimes represent two complementary configurations of topological bound states in the continuum. In the TBIC_1 regime, a σ-mode interface state is spectrally embedded within the π-mode bulk continuum. In contrast, the TBIC_2 regime corresponds to the reversed configuration, in which a π-mode interface state is embedded

within the σ-mode bulk continuum. In both cases, the localized interface state and the bulk continuum in which it is embedded belong to different orthogonal modal sectors.

The TF regime occurs when the σ-mode and π-mode interface states become spectrally coincident. Despite the coincidence of their eigenfrequencies, the two states retain their respective modal characters and do not directly hybridize because they belong to orthogonal mode sectors. This Topological Fano configuration is included here as part of the complete spectral evolution under geometric detuning, although it is not the primary focus of the present work.

To further resolve the spectral configurations shown in Fig. S5(a), representative values of Δl are selected in Fig. S5(b). The light-pink and light-blue branches correspond to the σ-mode and π-mode bulk states, respectively, whereas the red and blue markers denote the corresponding interface states. These representative spectra provide a direct view of how the interface-state frequencies move relative to the two bulk continua as the geometric detuning is varied. The spectra presented in Fig. 3(c) of the main text are selected from this complete evolution and focus on the representative configurations relevant to the continuum embedding of the TEP-BIC.

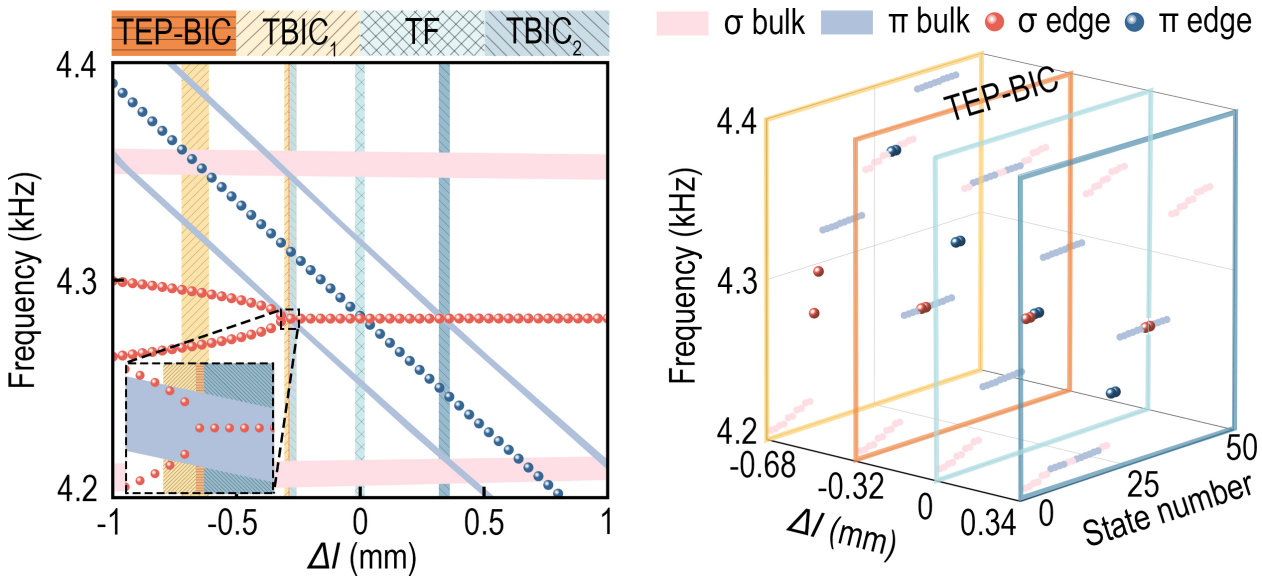


FIG. S5. Full spectral evolution under the geometric detuning $\Delta l = l_y - l_x$. (a) Evolution of the σ- and π-mode bulk spectra and their corresponding interface states as Δl is varied. The shaded regions indicate the TEP-BIC, TBIC_1, Topological Fano (TF), and TBIC_2 spectral configurations. In the TEP-BIC regime, the coalesced σ-mode interface state is embedded within the π-mode bulk continuum. TBIC_1 corresponds to a σ-mode interface state embedded in the π-mode bulk continuum, whereas TBIC_2 corresponds to a π-mode interface state embedded in the σ-mode bulk continuum. The TF regime denotes the spectral coincidence of the σ- and π-mode interface states without direct modal hybridization. The inset enlarges the corresponding local spectral evolution. (b) Finite-lattice eigenfrequency spectra at representative values of Δl. Light pink and light blue denote the σ- and π-mode bulk states, respectively, while red and blue markers denote the corresponding interface states.

8 Experimental Implementation of the Active-Feedback Gain Unit

The acoustic gain is implemented using a local active-feedback system, as shown in Fig. S6. Each active unit consists of a feedback microphone, a feedback controller, and a feedback loudspeaker coupled to the acoustic cavity through a horn. The feedback microphone detects the local acoustic pressure near the cavity opening, and the acquired signal is processed through the analog signal path of the feedback controller. The resulting electrical signal drives the feedback loudspeaker, which feeds acoustic energy back into the cavity and thereby modifies the effective acoustic dissipation.

The feedback controller uses an analog signal path for real-time acoustic feedback, while the digital circuitry is used only to set the feedback gain coefficient. No independent phase-control channel is introduced; the feedback polarity and phase relation are determined by the analog signal path. This configuration allows the feedback gain to be adjusted reproducibly without introducing an additional real-time digital signal-processing stage.

A total of twelve feedback controllers are used in the experimental lattice. They are connected to a central power and communication board, which provides a regulated 5-V DC supply and distributes the digital control commands used to set the gain coefficient of each controller. The central board is used only for power supply and gain-setting communication, whereas the acoustic feedback signal is processed locally by each feedback controller.

The feedback microphone is positioned close to the cavity opening, with its sensing surface parallel to the cavity side wall. The feedback loudspeaker (B1S automotive loudspeaker) is coupled to the cavity through an acoustic horn, whose narrow opening is also positioned near and parallel to the cavity side wall. By varying the feedback gain coefficient, the active-feedback loop compensates part of the intrinsic acoustic dissipation and provides a tunable non-Hermitian response. Experimentally, the feedback gain coefficient is the directly controlled quantity and is not assumed to have an exact one-to-one correspondence with the theoretical non-Hermitian parameter γ. The effective gain response of the active-feedback unit is characterized experimentally, as presented in Fig. 4(a) of the main text.

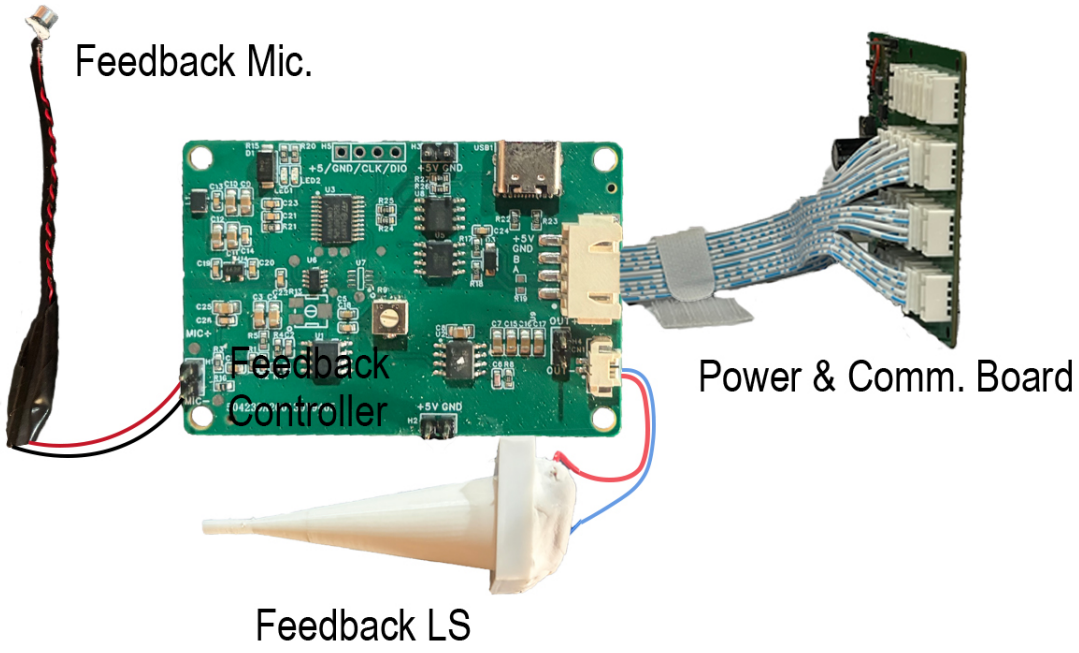


FIG. S6. Active-feedback system used to implement the acoustic gain unit, consisting of a feedback microphone, feedback controller, feedback loudspeaker, and a central power and communication board.

9 Spatial Mode Distributions in an Extended Acoustic Lattice

To further examine the spatial characteristics of the TEP-BIC in a larger system, we calculate the pressure-field distributions of the acoustic eigenstates in a finite lattice containing an increased number of supercells.

As shown in Fig. S7, the π-mode bulk eigenstates exhibit spatially extended distributions over the lattice, whereas the σ-mode states associated with the exceptional degeneracy remain strongly localized around the central a–b domain wall. The two σ-mode profiles coincide and exhibit pronounced spatial confinement, with their amplitudes decaying away from the interface.

These results demonstrate that the distinct spatial characteristics of the extended π-mode bulk states and the localized σ-mode TEP-BIC are preserved in a lattice with a larger number of supercells.



FIG. S7. Pressure-field distributions of the acoustic eigenstates in a finite lattice with an increased number of supercells. The upper panel shows the spatial distributions of the π-mode bulk states, which extend over the lattice. The lower panel shows the two coincident spatial profiles of the σ-mode states associated with the TEP-BIC, exhibiting strong localization around the central domain wall.

10 Spatial Responses at the Edge-State and Bulk-State Frequencies

To further investigate the spatial characteristics of the edge and bulk states, we calculate the acoustic responses of the 24-cavity lattice using finite-element frequency-domain simulations. An acoustic excitation is applied to the gain cavity immediately to the left of the central domain wall, and the resulting sound pressure responses are evaluated at each cavity position.

Two representative frequencies are selected for comparison: the frequency corresponding to the σ-mode edge state (ES) and a frequency within the σ-mode bulk band. Under the same excitation conditions, the spatial pressure distributions are extracted from the frequency-domain responses at these two frequencies, respectively.

Since the maximum sound pressure levels of the two responses differ by more than 100 dB under the same excitation, normalization using a common maximum would make the weaker response nearly indistinguishable in the spatial distribution. Therefore, the two responses are normalized independently to compare their respective spatial profiles.

Specifically, the sound pressure levels are converted into normalized squared-pressure magnitudes according to

$$\widetilde{I}_j^{(s)} = 10^{(L_j^{(s)} - L_{\max}^{(s)})/10}, \tag{111}$$

where $L_j^{(s)}$ denotes the simulated sound pressure level at the jth cavity for the selected frequency s ($s = \text{edge}, \text{bulk}$), and $L_{\max}^{(s)}$ is the maximum sound pressure level among the 24 cavity positions at the corresponding frequency.

As shown in Fig. S8, the response at the edge-state frequency exhibits pronounced spatial localization around the central domain wall, with the acoustic intensity decreasing rapidly toward the two ends of the lattice. At the selected bulk-band frequency, the system exhibits a different spatial response profile under the same excitation conditions.

For clarity, the independently normalized responses at the edge-state and bulk-band frequencies are displayed above and below the horizontal axis, respectively. The downward orientation of the bulk-frequency response is introduced solely for visual comparison and does not represent negative acoustic intensity.

It should be noted that the independent normalization is intended to highlight the spatial characteristics of the two responses rather than their absolute intensity difference.

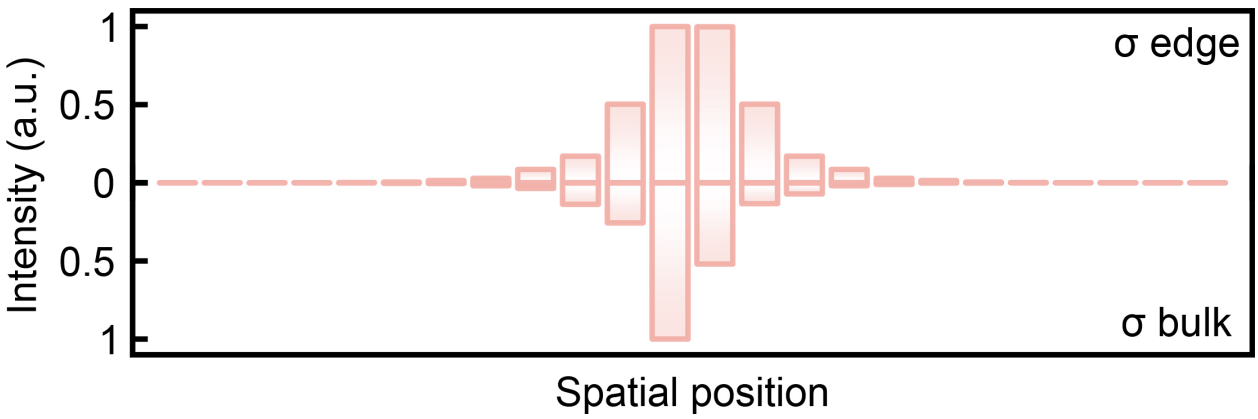


FIG. S8. Spatial acoustic responses of the 24-cavity lattice under excitation applied to the gain cavity immediately to the left of the central domain wall. The distributions are obtained from finite-element frequency-domain simulations at the σ-mode edge-state frequency (upper profile) and a representative σ-mode bulk-band frequency (lower profile). Because the peak sound pressure levels of the two responses differ by more than 100 dB under the same excitation, the squared-pressure magnitudes are normalized independently to their respective maxima for comparison of the spatial distributions. The bulk-frequency response is displayed below the horizontal axis solely for visual comparison.

11 Perturbation Setup for Anisotropic Sensitivity

To examine whether the topological, BIC, and exceptional-point properties remain individually addressable after being combined into the TEP-BIC, three different perturbation channels are introduced. The corresponding perturbation configurations are illustrated in Fig. S9. These perturbations act on different physical degrees of freedom and are designed to selectively probe the topological robustness, the symmetry-protected decoupling condition of the BIC, and the exceptional-point response, respectively.

The geometry perturbation δ_l modifies the local structural parameters without breaking the symmetry condition associated with the topological localization. It therefore provides a symmetry-preserving structural perturbation channel for probing the robustness inherited from the topological character of the localized state. In this perturbation channel, the structural parameters are varied while the symmetry condition relevant to the topological state is retained.

The position perturbation δ_y introduces a transverse displacement of the relevant structural element. In contrast to the geometry perturbation, this displacement breaks the modal-symmetry condition responsible for the symmetry-protected decoupling between the localized state and the bulk continuum. Consequently, the strict BIC condition is lifted once this symmetry is broken. The position perturbation therefore provides the perturbation channel used to probe the BIC component of the TEP-BIC.

The non-Hermitian perturbation δ_γ modifies the effective gain–loss contrast and directly perturbs the system around the non-Hermitian exceptional degeneracy. It therefore provides the perturbation channel used to probe the exceptional-point response. Unlike the two structural perturbations, δ_γ acts directly on the non-Hermitian degree of freedom responsible for the coalescence of the interface states.

For the numerical sensitivity analysis, the three perturbations are introduced as site-dependent random variations following a normal distribution with zero mean, with the perturbation magnitude controlled by the standard deviation of the corresponding distribution. Independent disorder configurations are used to examine the response of the TEP-BIC under different realizations. The corresponding experimental implementations are described separately in Section 12. In this way, the three perturbation protocols provide complementary channels for resolving the distinct physical ingredients contained in the same hybrid state: robustness associated with the topological localization, sensitivity to the symmetry breaking of the BIC condition, and the non-Hermitian response associated with the exceptional degeneracy.

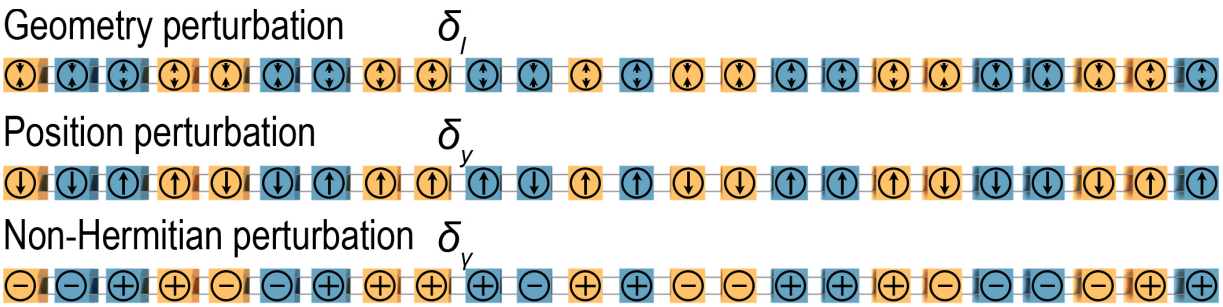


FIG. S9. Perturbation configurations used to selectively probe the three physical components of the TEP-BIC. The geometry perturbation δ_l modifies the local structural parameters without breaking the symmetry condition associated with the topological localization and is used to probe the topological robustness. The position perturbation δ_y breaks the modal-symmetry condition responsible for the symmetry-protected decoupling between the localized state and the bulk continuum, thereby lifting the BIC condition. The non-Hermitian perturbation δ_γ modifies the effective gain–loss contrast around the exceptional degeneracy and is used to probe the exceptional-point response.

12 Sensitivity Experiment Setting

The experimental setup used for the sensitivity measurements consists of the fabricated acoustic lattice, an acoustic excitation source, and a microphone-based data-acquisition system. The main measurement instrumentation is shown in Fig. S10(a), including a GRAS 46BD microphone, a National Instruments PXIe-4431 data-acquisition module, a power amplifier, and a computer for signal acquisition and processing. During the measurements, the acoustic pressure response is recorded at the domain wall of the finite lattice, where the TEP-BIC is spatially localized. The measured spectra are subsequently used to track the perturbation-induced evolution of the resonance response.

The acoustic samples are fabricated by stereolithography (SLA) with a nominal printing precision of 0.1 mm. Photosensitive resin is used as the printing material, with a density of $\rho_m = 1.16 \times 10^3$ kg/m^3, Young's modulus of $E_m = 2450$ MPa, and Poisson's ratio of $\nu_m = 0.41$. The outer-shell thickness of the fabricated samples is 3 mm. Representative samples used for the structural perturbation measurements are shown in Fig. S10(b). Separate sample sets are fabricated for the geometry perturbation δ_l and the position perturbation δ_y, with the dimensionless perturbation strength varied from 0.00625 to 0.05.

To compare the responses under different perturbation channels, a dimensionless perturbation coefficient is used to characterize the perturbation magnitude. For the structural perturbations, the corresponding dimensional variation is obtained by scaling the relevant reference geometric parameter with the prescribed dimensionless perturbation strength. The minimum structural variation used in the experiment is chosen to exceed the nominal printing accuracy, thereby reducing the influence of fabrication uncertainty.

The three perturbations are implemented through different experimental degrees of freedom. For the geometry perturbation δ_l, samples with the prescribed variation of the characteristic cavity dimension are used while the symmetry condition associated with the topological localization is preserved. For the position perturbation δ_y, the corresponding structural element is transversely displaced, thereby breaking the modal-symmetry condition protecting the BIC. These two structural perturbations are implemented by replacing the unperturbed lattice with the corresponding fabricated samples.

The non-Hermitian perturbation δ_γ is introduced by varying the gain setting of the active-feedback unit, thereby modifying the effective non-Hermitian contrast around the exceptional degeneracy. As described in the active-feedback implementation above, the feedback gain is the directly controlled experimental quantity and is not assumed to have an exact one-to-one numerical correspondence with the theoretical parameter γ. For each perturbation strength, the acoustic pressure spectrum at the domain wall is measured and used to quantify the corresponding spectral response.

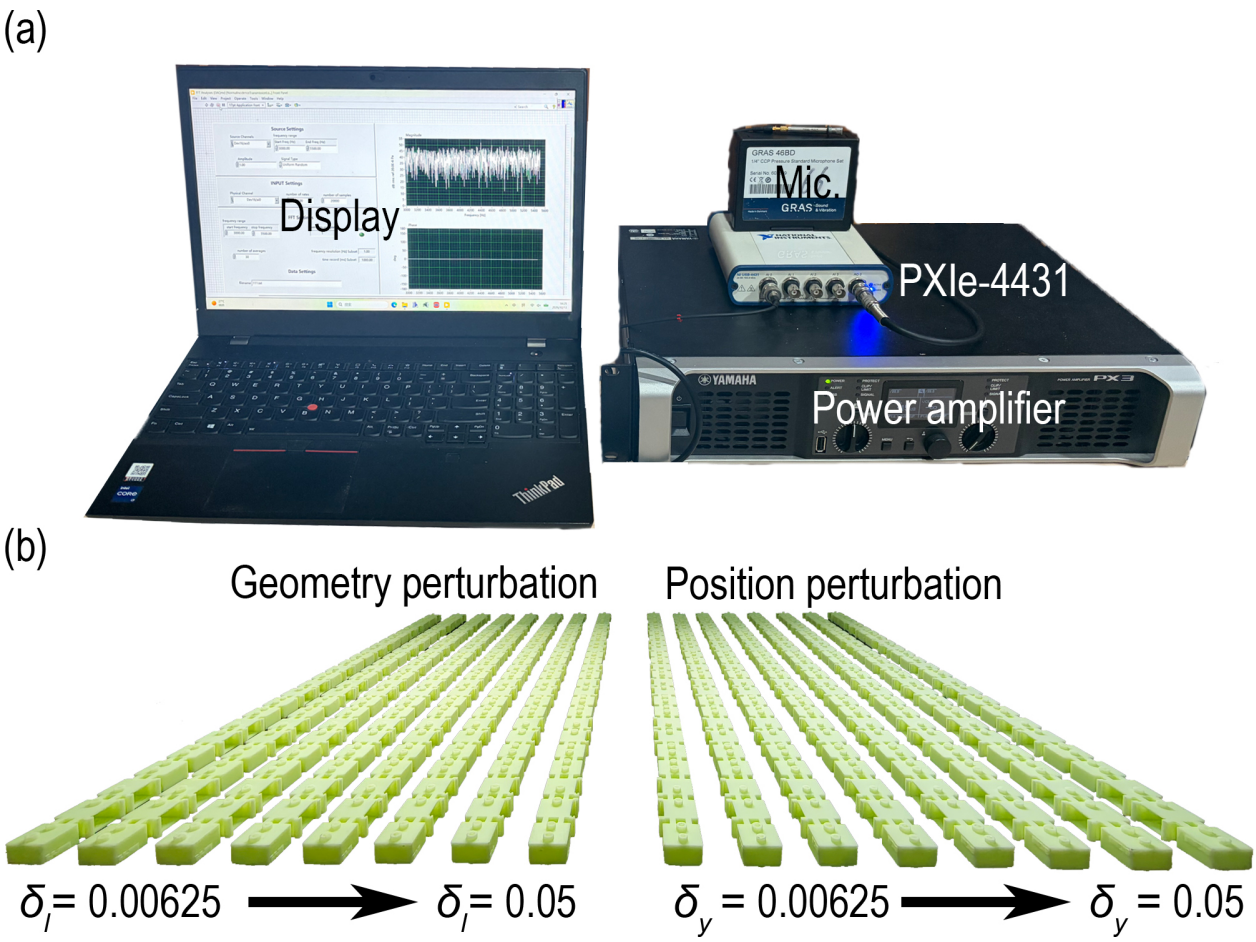


FIG. S10. Experimental instrumentation and fabricated samples used for the sensitivity measurements. (a) Main measurement instrumentation, including the computer for signal acquisition and processing, GRAS 46BD microphone, National Instruments PXIe-4431 data-acquisition module, and power amplifier. (b) Fabricated acoustic samples used for the geometry perturbation δ_l and position perturbation δ_y. For both structural perturbation channels, the dimensionless perturbation strength is varied from 0.00625 to 0.05, as indicated by the arrows.

13 Experimental Spectra for Sensitivity Extraction

Figure S11 shows the measured spectra used to extract the experimental frequency splitting presented in Fig. 5 of the main text. The responses under the geometry perturbation δ_l, position perturbation δ_y, and non-Hermitian perturbation δ_γ are measured at the domain wall for different perturbation strengths.

When two resonance peaks are resolved, their frequencies are identified, and the frequency splitting is calculated as

$$\Delta f = |f_1 - f_2|, \tag{112}$$

where f_1 and f_2 denote the extracted resonance frequencies. When only a single resonance peak can be resolved, the corresponding splitting is taken to be zero within the experimental resolution. The extracted values are used for the quantitative sensitivity comparison in Fig. 5(d) of the main text.

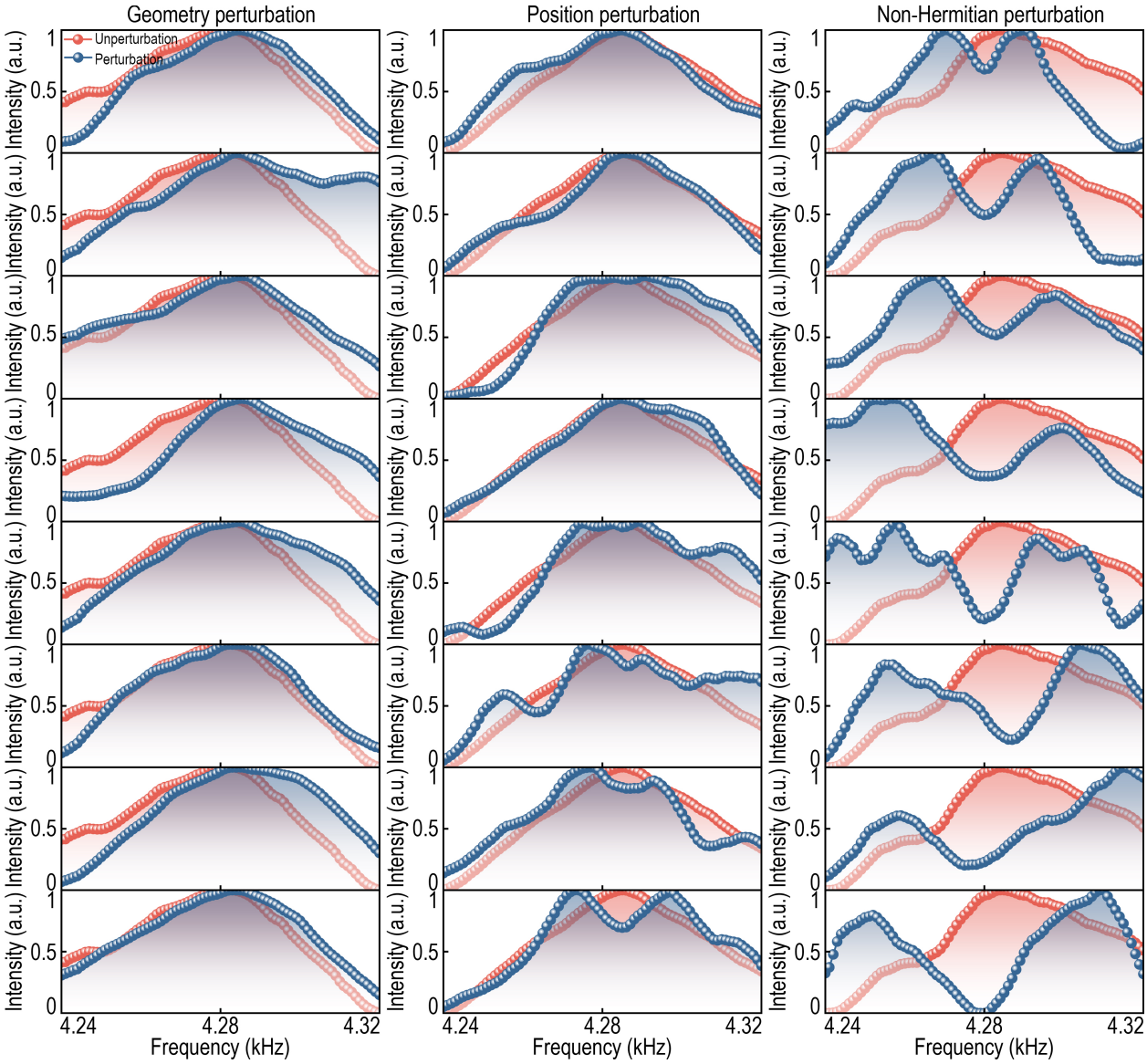


FIG. S11. Measured spectra used to extract the frequency splitting under the geometry perturbation δ_l, position perturbation δ_y, and non-Hermitian perturbation δ_γ.

14 Numerical Verification of Perturbation Responses

To supplement the experimental results, additional numerical calculations were performed under the three perturbation channels considered in the main text. The perturbations were introduced as normally distributed, site-dependent disorder, and representative realizations are shown in Fig. S12.

Under the geometry perturbation δ_l, the spectral response remains nearly unchanged, consistent with the robustness of the topological state under symmetry-preserving structural disorder. The position perturbation δ_y breaks the symmetry-protected modal decoupling and lifts the BIC condition, resulting in spectral splitting of the corresponding quasi-BIC states. In contrast, the non-Hermitian perturbation δ_γ directly perturbs the exceptional degeneracy and produces a pronounced splitting of the coalesced states. These numerical results reproduce the distinct perturbative responses discussed in the main text.

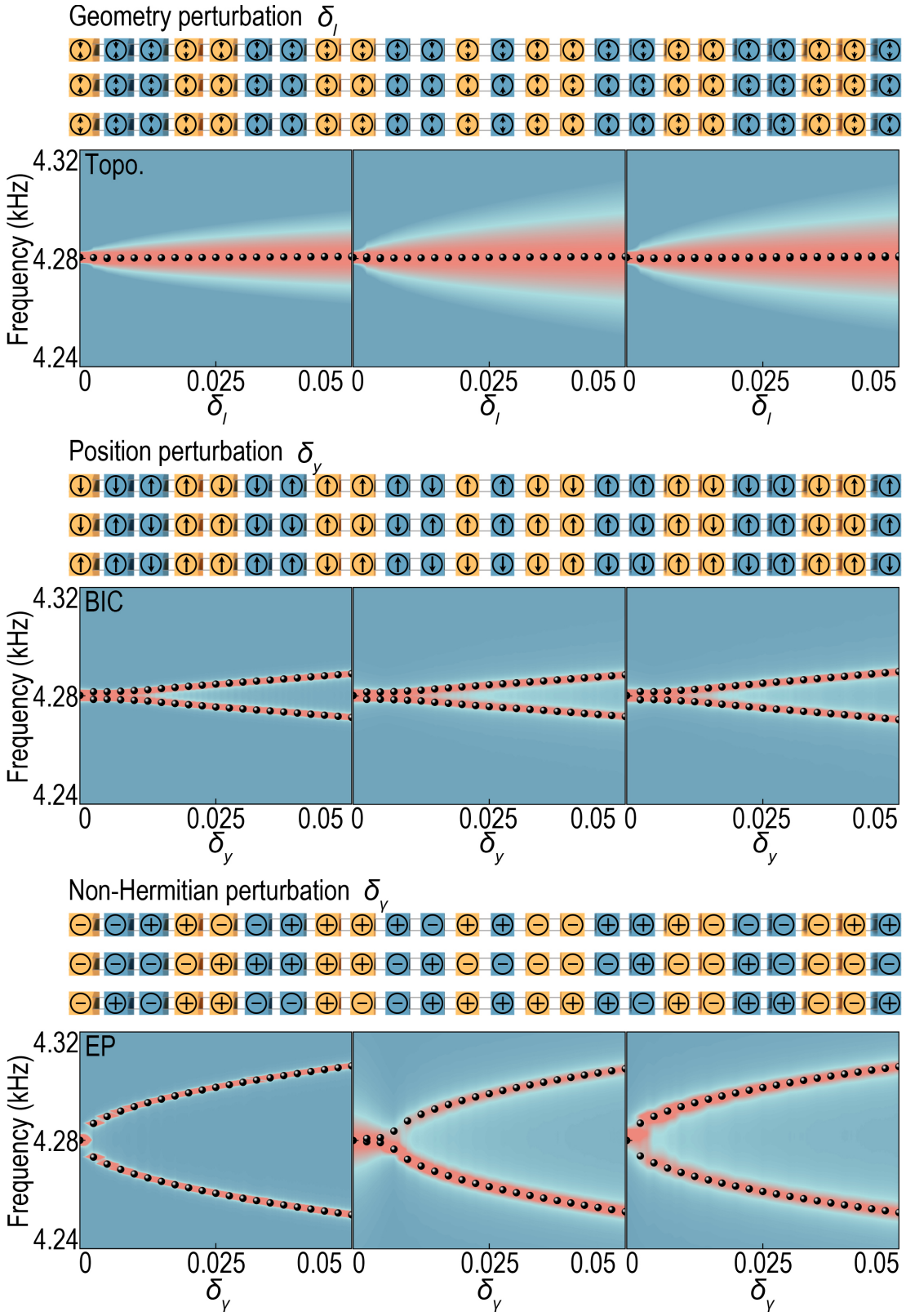


FIG. S12. Numerical responses of the TEP-BIC to the geometry perturbation δ_l, position perturbation δ_y, and non-Hermitian perturbation δ_γ. Three representative disorder realizations are shown for each case, with black circles marking the extracted eigenfrequencies.